

## Research Article

# Hybrid Recentering Energy Dissipative Device for Seismic Protection

**Wenke Tang and Eric M. Lui**

*Department of Civil and Environmental Engineering, Syracuse University, Syracuse, NY 13244-1240, USA*

Correspondence should be addressed to Eric M. Lui; [emlui@syr.edu](mailto:emlui@syr.edu)

Received 20 May 2014; Revised 30 July 2014; Accepted 1 August 2014; Published 23 September 2014

Academic Editor: Chris G. Karayannis

Copyright © 2014 W. Tang and E. M. Lui. This is an open access article distributed under the Creative Commons Attribution License, which permits unrestricted use, distribution, and reproduction in any medium, provided the original work is properly cited.

A hybrid recentering energy dissipative device that has both recentering and energy dissipation capabilities is proposed and studied in this paper. The proposed hybrid device, referred to as the hybrid shape memory alloy (SMA) recentering viscous fluid (RCVF) energy dissipation device, connects the apex of a chevron brace to an adjoining beam using two sets of SMA wires arranged in series on either side of the brace and a viscous fluid damper arranged in parallel with the SMA wires. The viscous damper is used because being a velocity-dependent device it does not exert any force that counteracts the recentering force from the SMA wires after the vibration of the frame ceases. In the numerical study, the Wilde's SMA constitutive model is used to model the SMA wires, and the Maxwell model is used to simulate the viscous fluid damper. To demonstrate the viability and effectiveness of the proposed hybrid device, comparative studies are performed on several single-story shear frames and a series of four-story steel frames. The results show that the frames equipped with the hybrid device have noticeably smaller peak top story displacements and residual story drifts when subjected to ground motions at three different intensity levels.

## 1. Introduction

The concept of performance-based seismic design (PBSD) was developed as a result of a series of devastating earthquakes that occurred in the 1990s [1–3]. The primary objective of PBSD is to provide guidelines and methods for siting, designing, constructing, and maintaining buildings so they have enough margin of safety to perform in a predictable manner under earthquake excitations. The Building Seismic Safety Council's (BSSC) National Earthquake Hazards Reduction Program (NEHRP) and the Structural Engineers Association of California's (SEAOC) Vision 2000 have set design objectives, prescribed design criteria, introduced analytical techniques for performance evaluation, and attempted to define the margin of safety for buildings designed and constructed in accordance with the proposed guidelines [4].

Figure 1 shows the SEAOC prescribed building performance levels for several types of buildings subjected to three different levels of ground motion. For essential buildings and structures (e.g., hospitals, fire stations, and dams) and hazardous facilities (e.g., nuclear power plants) to remain fully functional or operational after a frequent or rare earthquake

event, they need to have the capability to dissipate a sufficient amount of seismic energy during an earthquake and remain almost damage-free after the earthquake. Buildings without energy dissipative devices have to rely primarily on plastic or inelastic deformations, hysteresis, and localized damage of structural members to absorb the seismic energy. As the earthquake intensity increases, so do the inelastic deformations and damage level. On the other hand, buildings equipped with energy dissipative devices, such as viscoelastic, friction, and metallic dampers, often experience less inelastic deformations or damage due to their increased energy absorbing or damping capability. Depending on the severity of the earthquake, inelastic deformations—though relatively small—could still occur in buildings equipped with energy dissipative devices and result in postearthquake residual deflections or out-of-plumbness. Residual deformations are undesirable because they can dramatically affect the functionality of the buildings, making them appear unsafe to occupants, increasing the  $P$ -delta effect, impairing the buildings' structural performance to subsequent aftershocks, and significantly increasing the cost of repairs or replacements. Therefore, for buildings to achieve the performance levels of

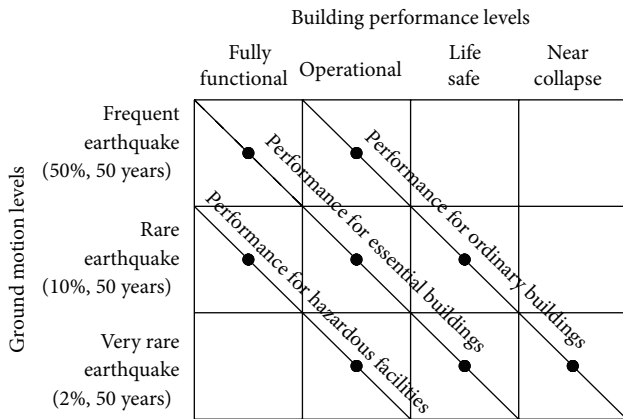


FIGURE 1: SEAOC Vision 2000 [5] performance-based seismic design levels.

fully functional or operational, two important seismic design objectives—an increase in energy dissipation and a reduction in residual deformations—must be met.

Recentering or self-centering is defined as the ability of a structure to return to its original configuration after a seismic event that may have caused noticeable inelastic deformations in some of the building's elements. In case of large residual deformations, recentering capability becomes vital if a building is to remain fully functional or operational after an earthquake.

Shape memory alloys (SMAs) are smart materials that exhibit certain unique and distinctive mechanical properties. Under a certain temperature range, SMAs can exhibit superelasticity effect in which they can undergo relatively large strain (up to 8%) [6] without showing permanent deformation and with a stress-strain curve that exhibits a distinctive plateau and a hysteresis. These features make SMAs ideal for use in recentering devices. However, SMAs cannot be solely relied upon for energy dissipation because of their relatively low damping effectiveness to cost ratio [7]. SMAs are novel and expensive materials, although their prices are expected to drop with an expanded market. At present, a more cost effective approach is to combine the self-centering feature of SMAs with the energy dissipative capability of other dampers in a hybrid device to regulate structural response to earthquake excitation.

In the past two decades, much research has been conducted to investigate the use of SMAs with various energy dissipative devices. In 2008, Shook et al. [8] investigated the behavior of a superelastic semiactive damping system which incorporates SMA wires with magnetorheological (MR) dampers. In 2008, Zhu and Zhang [9] conceived a recentering brace using SMA elements for recentering and a friction damper for energy dissipation. In 2010, Yang et al. [10] investigated a hybrid damping system composed of a set of recentering wires fabricated from SMA material, two energy-absorbing struts made from mild steel, and two high-strength steel tubes to guide the movement of the hybrid device. In 2011, Miller et al. [11] studied the application of SMA in buckling-restrained braces to achieve recentering and energy

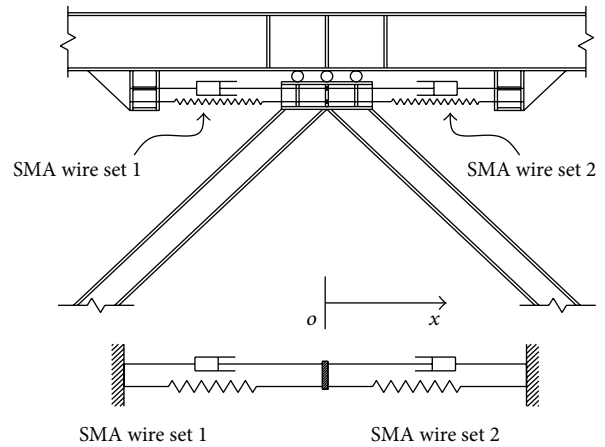


FIGURE 2: Conceptual design of a hybrid viscous SMA device.

dissipation. They proposed a self-centering buckling resistant brace (SC-BRB) consisting of a typical BRB component that dissipates earthquake energy and pretensioned superelastic NiTi shape memory alloy (SMA) rods that recenter the structure.

In this paper, a new device called the hybrid SMA recentering viscous fluid (RCVF) energy dissipation device is proposed. The hybrid device is made from two sets of SMA wires and a viscous fluid damper, the former for recentering and the latter for energy dissipation purposes. The proposed hybrid device is to be installed between the apex of a chevron brace and the beam above, as shown in Figure 2. Although there are two sets of SMA wires in the hybrid device, only one is effective at a given moment. When the beam and chevron brace move relative to each other, one of the SMA wire sets will be stretched and the other will become slack. The set that is being stretched will provide the recentering force for the frame. The reason for mounting the RCVF device on top of the chevron brace parallel to the beam as opposed to installing them along the axis of the braces is because this arrangement will subject the device to a larger relative displacement and velocities, hence allowing it to produce a larger restoring force and better energy dissipation for the frame.

Compared with other hybrid devices mentioned earlier, the force provided by the viscous fluid damper (modeled as two dashpots parallel to the springs that represent the SMA wires) is velocity dependent. After a seismic event when vibration ceases, the velocity of the frame drops to zero and so does the force in the viscous fluid damper. Unlike other energy dissipative devices discussed above, the viscous fluid damper imposes no extra resistance against recentering and thus has the advantage of increasing the energy dissipative capacity of the frame without compromising the recentering force provided to the frame by SMA wires.

In the following section, a brief description of SMA and fluid viscous damper, with emphasis on their constitutive modeling, will be given. Nonlinear quasistatic analyses are then carried out on a one-story shear frame having a RCVF device installed with different SMA wire sizes to demonstrate the recentering characteristics of the SMA wires. This will be

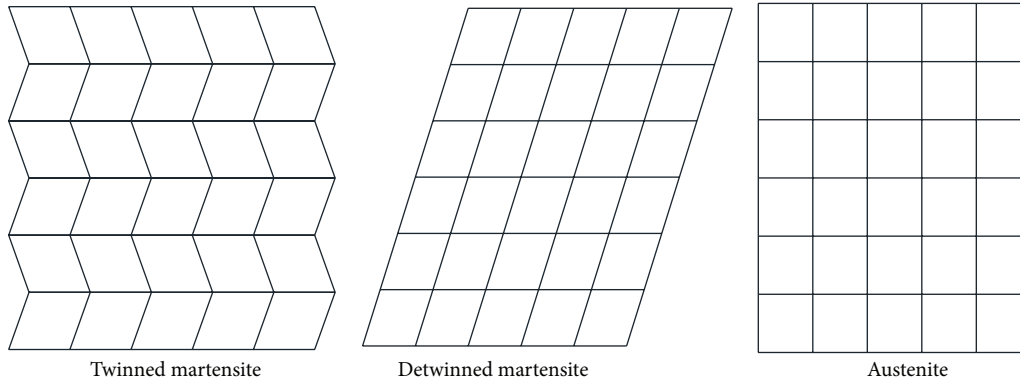


FIGURE 3: Different NiTi solid phases.

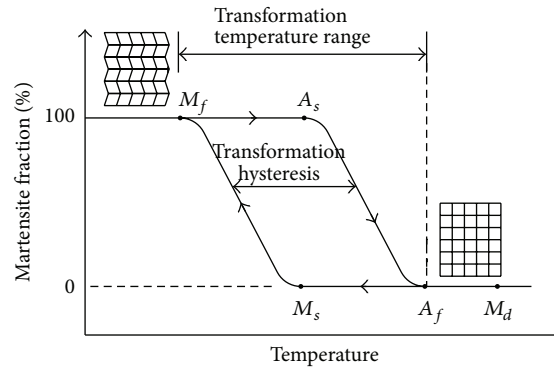


FIGURE 4: Temperature induced phase transformations of a typical SMA.

followed by a nonlinear time history analysis of the frame equipped with the RCVF device to demonstrate the viability and verify the efficacy of this device by examining the peak story displacement (PSD) and residual story drift (RSD) experienced by the frame under three sets of ground motions. For purpose of comparison, the same analyses are carried out for three additional frames identical in geometries to the RCVF frame, except that one has no device installed on it, another has only the SMA wire sets installed, and the third has only the viscous fluid damper installed. To further demonstrate the effectiveness of the proposed hybrid device in mitigating earthquake damage to buildings, a series of six four-story steel frames are analyzed using nonlinear time history procedure, and their peak top story displacements and residual story drifts are compared. Finally, the numerical analysis results are summarized and conclusions are made.

## 2. Behavior and Constitutive Model of SMA

Shape memory alloys (SMAs) are smart materials that exhibit two distinct properties desirable for earthquake resistant design, namely, the shape memory effect and the superelasticity effect. Under a certain temperature range, SMAs have the ability to revert to their original shape after they have been strained into the inelastic range. This is referred to as the shape memory effect. At another temperature range, SMAs can exhibit superelasticity effect in which they can undergo relatively large strain (up to 8%) [6] without showing

permanent deformation and with a stress-strain curve that exhibits a distinctive plateau and a hysteresis.

The shape memory and superelasticity effects of SMAs are related to their metallurgical structures. SMAs can exist in two different crystal phases. For NiTi (acronym for nickel titanium or nitinol) alloy, these two phases are martensite and austenite, and, depending on the crystal orientation direction, martensite can exist in two forms: twinned or detwinned (Figure 3). Martensite is stable at low temperatures and high stresses, while austenite is stable at high temperatures and low stresses. These two phases have different mechanical properties and could be transformed into each other under different stress and thermal conditions. Therefore, SMAs can exhibit versatile properties when circumstances change.

For temperature induced solid-to-solid phase transformations, there are four characteristic temperatures at which phase transformations occur: (1) the austenite start temperature,  $A_s$ , where the material starts to transform from twinned martensite to austenite, (2) austenite finish temperature,  $A_f$ , where the material is completely transformed to austenite, (3) the martensite start temperature,  $M_s$ , where austenite begins to transform into twinned martensite, and (4) the martensite finish temperature,  $M_f$ , where the transformation to martensite is completed (Figure 4).  $M_d$  in the figure represents a critical temperature above which austenite will become stable and no solid-to-solid phase transformation is likely to occur. Different SMAs have different transformation temperature ranges and hystereses.

Within a given temperature range, the solid-to-solid phase transformations can occur as a result of applied stresses. Stress induced phase transformation gives rise to different mechanical behavior at different temperature ranges.

When the temperature is below  $M_f$ , SMA such as NiTi is in its twinned martensite phase. If a stress above a critical level is applied, it undergoes a phase transformation to detwinned martensite and stays in this phase even upon removal of the applied load. The material can regain its initial shape only when it is heated to a temperature above  $A_f$ . Heating the SMA material above  $A_f$  not only results in shape recovery but also leads to the formation of the austenite phase. Through subsequent cooling, the SMA transforms to its initial twinned martensite phase with little or no residual deformation. This phenomenon is referred to as the shape memory effect—that is, the ability of an SMA material to recover its original shape through thermal cycling.

On the other hand, when the temperature is above  $A_f$ , the SMA is in its austenite phase. When a sufficiently high stress is applied, the SMA transforms into detwinned martensite. Upon removal of the load, a reverse transformation to the austenite phase takes place, with the material undergoing shape recovery and exhibiting a noticeable hysteresis loop. This phenomenon is referred to as the superelasticity effect—that is, the recovery of large strain as a result of the stress-induced phase transformations under a constant temperature. If the temperature is below  $A_f$  but above  $M_f$ , there will only be a partial shape recovery after the load is removed, and the remaining strain could only be recovered via a heating and cooling cycle. Finally, when the temperature is above  $M_d$ , the SMA is stable in its austenite phase and will behave like an ordinary metal that undergoes plastic deformation when stressed beyond a certain limiting value (Figure 5).

Certain features of SMAs make them quite desirable in meeting the requirements for performance-based seismic design. In the martensite phase, SMAs such as NiTi possess good hysteresis and through thermal cycling exhibit shape memory effect, which can help restore a structure to its original undeformed state after being stressed. In the austenite phase, although the hysteresis is reduced, SMAs can undergo large deformation with little or no residual strain. This superelasticity effect can be used to assist with the recentering of a structure after a seismic event. The hysteresis also contributes to the structure's energy dissipation capacity. Because the superelasticity effect is applicable over a wide temperature range, it is effective in extreme temperature conditions. For instance, by adjusting the alloy contents, the austenite finish temperature of NiTi could be as low as  $-50^\circ\text{C}$  [12]; a copper based SMA, CuAlBe, exhibits superelastic behavior at a temperature range of  $-65^\circ\text{C}$  to  $180^\circ\text{C}$ ; a newly discovered ferrous based SMA called NCATB has an austenite finish temperature of  $-62^\circ\text{C}$  [13]. Moreover, a number of SMAs have excellent fatigue and corrosion resistance and exhibit stable mechanical property after a training process (i.e., controlled cyclic loading and unloading of the SMA component at the expected working temperature until its mechanical property stabilizes [14]). All these attributes make SMAs rather suitable for use in devices that enhance the performance of structures under earthquake excitations.

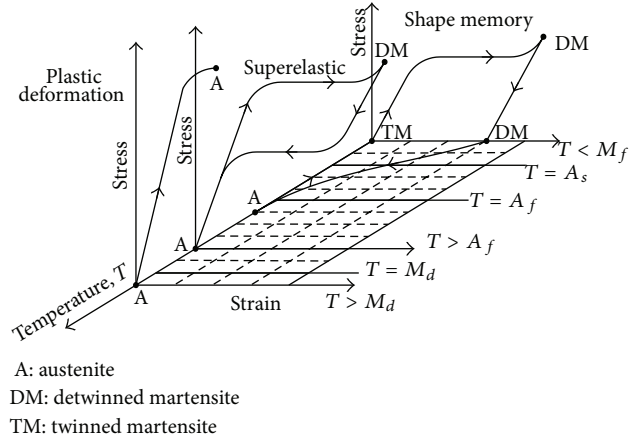


FIGURE 5: Stress-strain temperature diagrams of NiTi at different temperatures.

When compared with other SMAs, Dolce et al. [15] considered NiTi, with near equiatomic composition subjected to cold working and annealing treatments, as the most suitable SMA for use in passive control devices because of its better superelastic properties, lower sensitivity to temperature change, and higher resistance to corrosion and fatigue. Table 1 shows a comparison of the mechanical properties of NiTi [6] with steel and aluminum alloys. As can be seen, NiTi possesses properties that are either comparable to or better than those of steel and aluminum alloys.

To fully utilize SMAs' potential in a variety of engineering fields and to facilitate the development of computational models suitable for numerical analysis, a number of SMA constitutive models have been developed. Because the most common forms of SMA used in current civil engineering research and applications are SMA bars and wires in their austenite state, one-dimensional phenomenological superelastic models are often considered suitable. In 2004, Li et al. [16] proposed a piecewise linear force-displacement relationship for superelastic SMA wires. In 2005, Andrawes and DesRoches [17] developed a simplified superelastic SMA model by combining three different types of element in DRAIN-2DX. As early as 1994, Graesser and Cozzarelli [18] proposed a one-dimensional strain rate independent model for hysteretic behavior of SMA. The Graesser and Cozzarelli model is a relatively simple expression with parameters that can easily be calibrated. However, their model excludes the martensitic hardening characteristics of SMA under large amplitudes, which are critical for structural safety protection under extreme events. In 2000, Wilde et al. [19] made improvements to the Graesser and Cozzarelli model [18] by introducing parameters to describe the material behavior after the completion of phase transformation as well as by simulating a smoother transition between the elastic branch and the superelastic plateau of the stress-strain curve. The Wilde model is illustrated in Figure 6.

The Wilde SMA superelastic model is expressed as

$$\dot{\sigma} = E_A \left[ \dot{\epsilon} - |\dot{\epsilon}| \left( \frac{\sigma - \beta}{Y_A} \right)^n \right] \cdot u_I(\epsilon) + E_M \cdot \dot{\epsilon} \cdot u_{II}(\epsilon) + (3a_1 \dot{\epsilon} \epsilon^2 + 2a_2 \text{sign}(\epsilon) \dot{\epsilon} \epsilon + a_3 \dot{\epsilon}) \cdot u_{III}(\epsilon), \quad (1)$$

TABLE 1: Comparison of NiTi shape memory alloy with steel and aluminum alloys.

| Property               | NiTi   | Steel                 | Aluminum alloys                |
|------------------------|--|-----------------------|--------------------------------|
| Elastic modulus        | $8.7 \times 10^4$ MPa (austenite)<br>$1.4 \sim 2.8 \times 10^4$ MPa (martensite) | $200 \times 10^3$ MPa | $(70 \sim 73) \times 10^3$ MPa |
| Yield strength         | 200~700 MPa (austenite)<br>70~140 MPa (martensite)                               | 250~690 MPa           | 230~500 MPa                    |
| Tensile strength       | 900 MPa (fully annealed)<br>2000 MPa (work hardened)                             | 400~760 MPa           | 260~570 MPa                    |
| Recoverable elongation | 8%   | 0.125~0.345%          | 0.3~0.7%                       |
| Elongation at failure  | 25~50% (fully annealed)<br>5~10% (work hardened)                                 | 17~21%                | 11~19%                         |

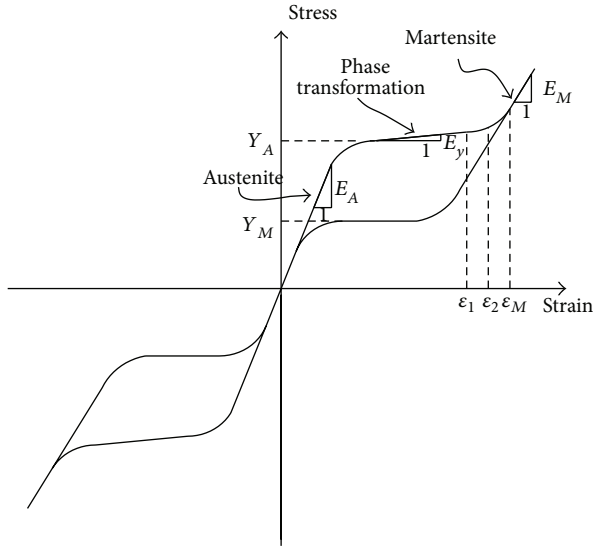


FIGURE 6: Schematic SMA stress-strain relationship as described by the Wilde model [19].

where the functions  $u_I(\epsilon)$ ,  $u_{II}(\epsilon)$ , and  $u_{III}(\epsilon)$  are given by

$$u_I(\epsilon) = 1 - u_{II}(\epsilon) - u_{III}(\epsilon), \quad (2a)$$

$$u_{II}(\epsilon) = \begin{cases} 1, & |\epsilon| \geq \epsilon_M, \\ 0, & \text{otherwise,} \end{cases} \quad (2b)$$

$$u_{III}(\epsilon) = \begin{cases} 1, & \dot{\epsilon} \cdot \epsilon > 0, \quad \epsilon_1 < |\epsilon| < \epsilon_M, \\ 0, & \text{otherwise,} \end{cases} \quad (2c)$$

$$\text{sign}(\epsilon) = \begin{cases} 1, & \text{if } \epsilon > 0, \\ 0, & \text{if } \epsilon = 0, \\ -1, & \text{if } \epsilon < 0, \end{cases} \quad (3)$$

in which, with reference to Figure 6,  $Y_A$  is the loading yield stress,  $\epsilon_M$  is the strain when the transformation from austenite to martensite is complete, and  $n$  is a parameter to control the shape of the stress-strain curve. The second term in (1) that contains  $E_M$  models the elastic behavior of martensite and is nonzero only when  $|\epsilon| > \epsilon_M$ . The last term in (1) controls the slope transition from  $E_y$  to  $E_M$  and is nonzero only when the total strain  $|\epsilon|$  is within the  $(\epsilon_1, \epsilon_M)$

transition region during loading.  $\epsilon_1$  and  $\epsilon_2$  are curve fitting points, and the constants  $a_1, a_2, a_3$  control the smoothness of the transition. The other parameters,  $\beta$  and  $\epsilon_{in}$ , as given below are the same as those in the Graesser and Cozzarelli model as follows:

$$\beta = E_A \alpha \left\{ \epsilon_{in} + f_T |\epsilon|^c \text{erf}(a\epsilon) [H(-\epsilon\dot{\epsilon})] \right\}, \quad (4)$$

$$\epsilon_{in} = \epsilon - \frac{\sigma}{E_A}, \quad (5a)$$

$$\alpha = \frac{E_y}{E_A - E_y}, \quad (5b)$$

$$H(x) = \begin{cases} 1, & x \geq 0, \\ 0, & x < 0. \end{cases} \quad (6)$$

The coefficients  $f_T, a$ , and  $c$  are material constants controlling the recovery of the elastic strain during unloading,  $E_A$  and  $E_y$  are slopes in the different regions of the stress-strain curve as shown in Figure 6, erf is the error function, and  $H$  is the Heaviside or unit step function.

Other researchers have made further modifications to the Graesser-Cozzarelli and the Wilde models. For instance, Qian et al. [20] improved the Graesser-Cozzarelli [18] model to enable it to describe the martensitic hardening characteristic of SMAs, and Zhang and Zhu [21] modified the Wilde model to enhance its stability in numerical simulation and improve the computation efficiency. However, these models introduce an additional layer of complexity to the problem. Therefore, with consideration of both simplicity and accuracy, the Wilde [19] model is adopted in the present study.

It should be noted that none of the aforementioned superelastic SMA models explicitly incorporate the loading rate and temperature effects in the modeling. As a result, they need to be calibrated with test data with a loading rate comparable to that of an earthquake loading. Room temperature is assumed during the calibration process.

Based on Table 1, the elastic moduli of SMA in the austenite and martensite states are selected as  $E_A = 8.7 \times 10^4$  MPa and  $E_M = 2.0 \times 10^4$  MPa, respectively. The strain limit for the superelastic range is  $\epsilon_M = 0.08$ , and the points defining the transition from  $E_y$  to pure martensite elastic response are  $\epsilon_1 = \epsilon_M - 0.03$  and  $\epsilon_2 = (\epsilon_M + \epsilon_1)/2$ . The loading ‘‘yield’’ stress, which is the forward transformation stress from austenite to

martensite, is assumed to be  $Y_A = 410$  MPa; the unloading “yield” stress, which is the martensite yield strength, is assumed to be  $Y_M = 140$  MPa. The parameters used to control the shape of the superelastic loop are  $n = 3$ ,  $\alpha = 0.009$ ,  $c = 0.001$ ,  $a = 900$ , and  $f_T = 0.70$ . The transition curvature controlling parameters used are  $a_1 = 9.83 \times 10^6$ ,  $a_2 = -7.19 \times 10^5$ , and  $a_3 = 0$ . The selected parameters of SMA correspond to an alloy with good superelastic behavior.

### 3. Viscous Fluid Damper

Viscous fluid dampers (VFDs) used in structures work very much like automotive shock absorbers except they can handle much larger forces. A typical viscous fluid damper consists of a cylinder and a stainless-steel piston. The cylinder is filled with an incompressible silicone fluid that has stable properties over a wide range of operating temperatures. VFDs in civil engineering applications can be designed to have a wide operational temperature range, from  $-40^\circ\text{C}$  to  $70^\circ\text{C}$  [22]. It is the transfer of fluid from chamber to chamber and the resulting pressure difference that provides the damping force. The mechanical construction and orifice properties can be varied to obtain the desired damper properties.

When implemented as part of the lateral load resisting system of a structure, VFDs can greatly improve the structural response to seismic loads. They do this by increasing the equivalent damping ratio from 2%–5%, typical for buildings, to 20%–30% of critical damping, which can greatly reduce the building’s acceleration and displacement. Without these devices, a building with only about 2%–5% of critical damping must rely on the inherent damping capability of the structure to dissipate the input energy. If the applied force or the input energy is large enough as in a typical strong motion earthquake, the building can easily exhaust its inherent damping and has to undergo inelastic deformations to absorb the earthquake energy. VFDs have been used for regulating structural response for both new buildings and retrofitting existing buildings.

The differential equation that describes the force-velocity relationship of a viscous fluid damper [22] is given by

$$F + \lambda \dot{F} = C_0 \dot{u}^{\alpha_d}, \quad (7)$$

where  $F$  is the output force,  $\lambda$  is the relaxation time,  $C_0$  is the damping constant at zero frequency,  $\dot{u}$  is the velocity the viscous fluid damper is subjected to, and  $\alpha_d$  is the damping exponent, which is dependent on the shape of the piston head. For typical structural applications, the second term on the left hand side of the equation can be neglected. Additionally, although  $\alpha_d$  may vary from 0.3 to 1.0, unless specific response limitations above a given velocity are necessary, a value of  $\alpha_d = 1$  is often used for the design of VFDs for structural applications. In view of this, the VFD constitutive model is simplified as

$$F = C_0 \dot{u}. \quad (8)$$

The damping constant  $C_0$ , typically given in units of  $\text{kN}\cdot\text{s}/\text{m}$ , is specified by the design engineer and, along with information on the maximum velocity for the building,

will allow the manufacturer to supply the necessary equipment. Depending on the damping requirements of the building, the resulting force may range anywhere from 8.9 kN to 8900 kN.

Over the years, many research studies concerning the effect of VFDs on the seismic performance of building structures have been conducted. It was found that VFDs reduce not only story drifts and story shear forces but also column bending moments, while introducing additional column axial forces which are out-of-phase with the bending moments [22]. Thus, it has been suggested that this behavior prevents the compression failure of weak columns in retrofitting applications. Other researchers focused on the optimization aspect of VFD application in moment resisting frames. For instance, Martinez-Rodrigo and Romero [23] proposed a simple methodology leading to an optimum retrofitting option for moment resisting frames with linear and nonlinear VFDs. Uriz and Whittaker [24] found that using VFDs with an equivalent viscous damping of 40% of critical damping resulted in a reduction in the displacement of the frame by a factor exceeding two. Dicleli and Mehta [25] recommended that using VFDs with damping ratios within the range of 10% ~ 30% was very effective for the seismic design and retrofit of concentrically braced frames with a large number of stories subjected to high intensity ground motions, but any increase beyond 30% would not appreciably enhance the seismic performance of the structure.

Based on the results of these studies, a damping coefficient that corresponds to a damping ratio of approximately 15% will be used for the nonlinear time history analysis of the one-story shear frames and the four-story steel frames to be discussed in later sections.

### 4. Shear Frames

The one-story shear frames used for the present study are shown in Figure 7. SF-N is a shear frame without any recentering or damping device, SF-VF and SF-RC are shear frames having the chevron brace equipped with only the viscous fluid damper and with only the SMA recentering device, respectively, and SF-RCVF is the chevron-braced shear frame equipped with the hybrid SMA recentering viscous fluid energy dissipative device.

The height  $h$  of the frames is 3.6 m, and the bay width  $L$  is 6.0 m. The beam is assumed to be infinitely stiff, and the columns are  $W150 \times 22.5$  section with a moment of inertia  $I_c = 12.2 \times 10^6 \text{ mm}^4$ , a cross sectional area  $A_c = 2860 \text{ mm}^2$ , and a plastic modulus of  $Z_c = 177 \times 10^3 \text{ mm}^3$ , made from ASTM A36 steel with a modulus of elasticity of  $E = 2 \times 10^5 \text{ MPa}$  and a minimum specified yield stress  $\sigma_y = 248 \text{ MPa}$ . The braces are  $HSS127 \times 127 \times 6$  section with a moment of inertia  $I_c = 6.65 \times 10^6 \text{ mm}^4$ , a cross sectional area  $A_c = 2.77 \times 10^3 \text{ mm}^2$ , and a plastic modulus of  $Z_c = 124 \times 10^3 \text{ mm}^3$ , made from ASTM A500 Grade B steel with yield strength of 318 MPa.

In the quasistatic analysis, a column plastic hinge is assumed to have formed when the bending moment in any cross section along the member length reaches  $M_{pc} = \sigma_y \times Z_c = 43.9 \text{ kN}\cdot\text{m}$ . A simple plastic analysis of the SF-N frame

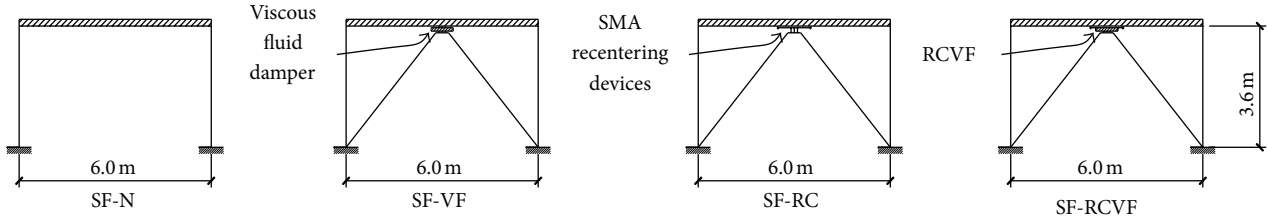


FIGURE 7: One-story shear frames.

gives the plastic limit lateral load of the structure as  $F_{cr} = 4M_{pc}/L = 48.8 \text{ kN}$ , when plastic hinges form at the ends of each column. The displacement of the rigid beam when this occurs is  $D_{cr} = 0.0389 \text{ m}$ , calculated by dividing  $F_{cr}$  by the lateral stiffness of the SF-N frame  $K_{SF-N} = 2 \times 12EI_c/h^3 = 1.255 \times 10^3 \text{ kN/m}$ .

The length of the SMA wires is determined based on their limiting strain. Although SMA wires have an elongation capability of up to 8% in a pseudoelastic state, martensite hardening starts to occur when its strain exceeds 8%. As a result, a strain limit less than 8% is often used. In the present study, the SMA wires are designed so that when plastic hinges form in the SF-N frame, the corresponding strain in the wires (if they were present) will be less than 5%. The length of the SMA wires is thus determined to be  $L_{SMA} = 800 \text{ mm}$  as shown in the calculation below:

$$\frac{D_{cr}}{L_{SMA}} = \frac{38.86}{800} = 4.86\% \approx 5\%. \quad (9)$$

Because the shear frame is modeled as a single degree-of-freedom system, the lateral stiffness of the SF-RCVF and SF-RC frames can be obtained as the sum of the lateral stiffness  $K_{SF-N}$  of the SF-N frame and the axial stiffness of one set of SMA wires. The viscous fluid damper is a velocity dependent energy dissipative device so it does not contribute any stiffness to the system.

Each frame is assumed to be part of an office building, and a seismic weight [26] of 3564 kg is assumed for all calculations.

## 5. Nonlinear Quasistatic Analysis of Shear Frames

In a quasistatic loading scenario, the frame experiences zero velocity. As a result, the fluid viscous damper, whose force is proportional to velocity, is ineffective and does not dissipate any energy. Therefore, under static loading, the SF-N and SF-VF frames will have the same response, and the SF-RC and SF-RCVF will behave the same as long as the recentering components are identical. In this section, a SF-N frame and a series of SF-RCVF frames with different SMA wire sizes are subjected to a static load that varies in magnitude to study the recentering effect of the SMA wires. The shear frames analyzed in this section are used for illustrative purpose only. In reality, frames are often designed using the strong column weak beam concept.

The quasistatic loading protocol used is shown in Figure 8. It is a displacement based loading process, with  $D$  referring to the horizontal displacement of the beam in the

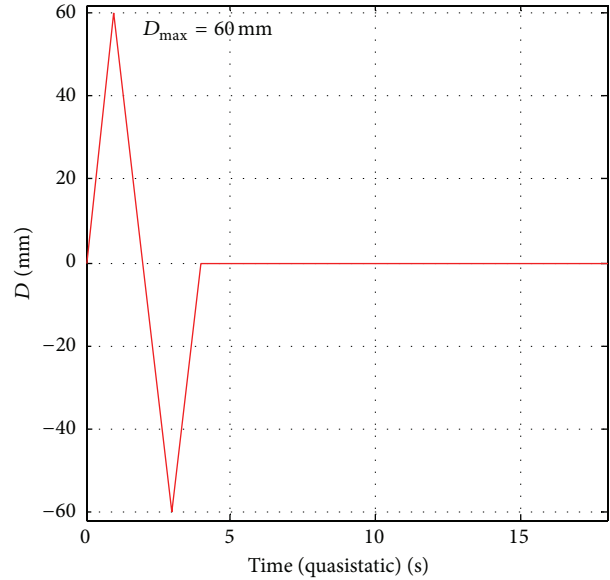


FIGURE 8: Loading protocol used for the quasistatic analysis.

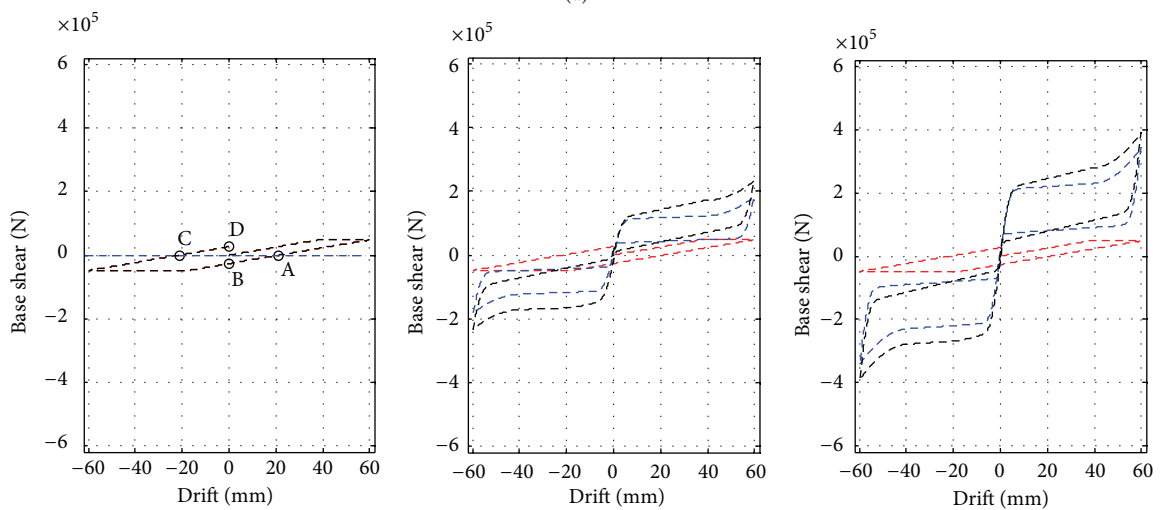
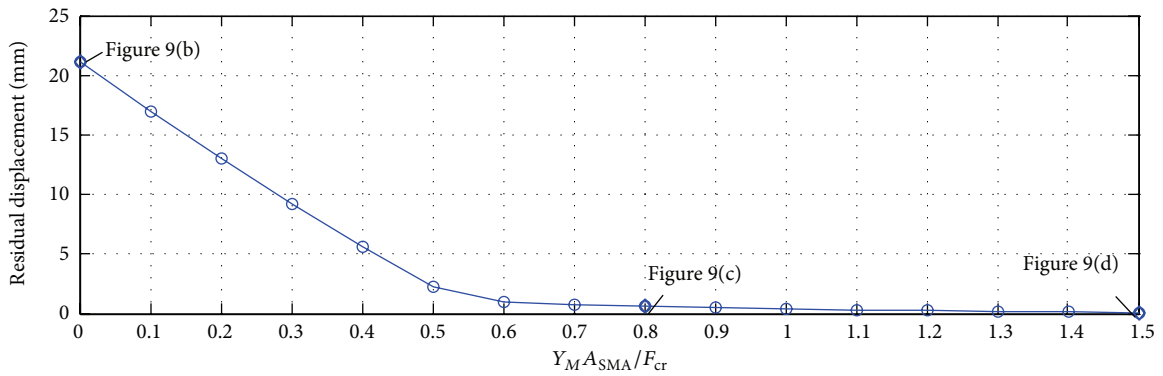
shear frame, and is considered positive when the frame sways to the right. All the frames are subjected to one cycle of loading and unloading in each direction. The largest displacement experienced by the beam is denoted by  $D_{max}$  and, in this analysis, is set at 60 mm, which corresponds to a story drift ratio of 1.7%.

A parametric study using different SMA wire cross-sectional areas is performed. The cross-sectional areas  $A_{SMA}$  used are given in the second column of Table 2, and their corresponding initial stiffness  $K_{SMA,I}$  is given in the third column. The initial stiffness of the wires normalized by the lateral stiffness of the SF-N frame  $K_{SF-N}$  is given in the fourth column, and the unloading “yield” force  $Y_M A_{SMA}$  normalized by the plastic limit load  $F_{cr}$  of the SF-N frame is given in the last column.

The lateral residual displacements of these SF-RCVF frames plotted against  $Y_M A_{SMA}/F_{cr}$  are shown in Figure 9(a). From the figure, it can be seen that as  $A_{SMA}$  increases, the residual displacement of the SF-RCVF frame decreases. When  $Y_M A_{SMA}/F_{cr}$  reaches approximately 0.6, the residual displacement tends toward zero. In Figures 9(b), 9(c), and 9(d), base shear versus frame drift is plotted for cases number 0, number 8, and number 15 that correspond to  $A_{SMA}$  equal to  $0 \text{ mm}^2$ ,  $276.21 \text{ mm}^2$ , and  $517.90 \text{ mm}^2$ , respectively. Each plot consists of three curves: the red dashed lines representing

TABLE 2: Cross-sectional area of SMA wires used in the parametric study.

| SF-RCVF number | $A_{SMA}$ (mm <sup>2</sup> ) | $K_{SMA,I} = E_A A_{SMA} / L_{SMA}$ (10 <sup>3</sup> kN/m) | $K_{SMA,I} / K_{SF-N}$ | $Y_M A_{SMA}$ (kN) | $Y_M A_{SMA} / F_{cr}$ |
|----------------|------------------------------|--|------------------------|--------------------|------------------------|
| 0              | 0.00                         | 0.0  | 0.00                   | 0.0                | 0                      |
| 1              | 34.53                        | 3.8  | 2.99                   | 5                  | 0.1                    |
| 2              | 69.05                        | 7.5  | 5.98                   | 10                 | 0.2                    |
| 3              | 103.58                       | 11.3   | 8.97                   | 15                 | 0.3                    |
| 4              | 138.11                       | 15.0   | 11.97                  | 19                 | 0.4                    |
| 5              | 172.63                       | 18.8   | 14.96                  | 24                 | 0.5                    |
| 6              | 207.16                       | 22.5   | 17.95                  | 29                 | 0.6                    |
| 7              | 241.69                       | 26.3   | 20.94                  | 34                 | 0.7                    |
| 8              | 276.21                       | 30.0   | 23.93                  | 39                 | 0.8                    |
| 9              | 310.74                       | 33.8   | 26.92                  | 44                 | 0.9                    |
| 10             | 345.26                       | 37.5   | 29.91                  | 48                 | 1.0                    |
| 11             | 379.79                       | 41.3   | 32.91                  | 53                 | 1.1                    |
| 12             | 414.32                       | 45.1   | 35.90                  | 58                 | 1.2                    |
| 13             | 448.84                       | 48.8   | 38.89                  | 63                 | 1.3                    |
| 14             | 483.37                       | 52.6   | 41.88                  | 68                 | 1.4                    |
| 15             | 517.90                       | 56.3   | 44.87                  | 73                 | 1.5                    |



(b) (c) (d)

--- SF-N  
 --- SMA wires  
 --- SF-RCVF

FIGURE 9: Force displacement diagrams of SF-N and SMA wires in three SF-RCVFs.

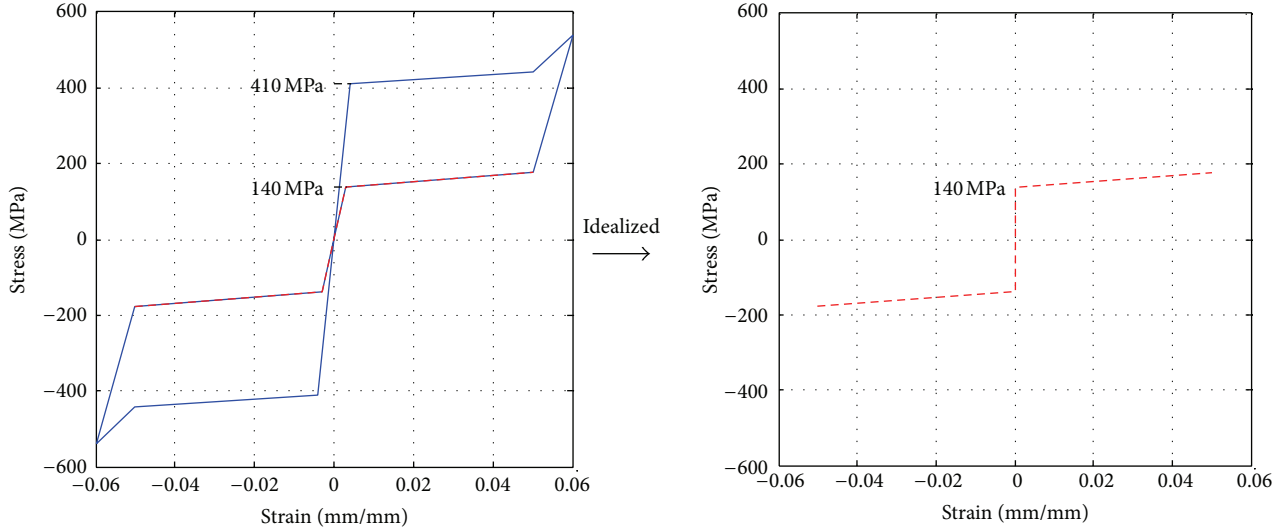


FIGURE 10: Piecewise linear stress-strain idealization of SMA wires.

the contribution of the bare frame, the blue dashed line representing the contribution of the SMA wires, and the black dotted lines representing the sum of the two.

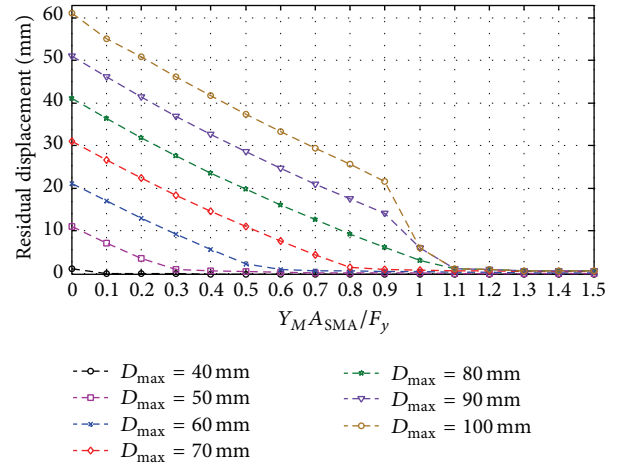
From Figure 9(b), we can see that when the cross-sectional area of the SMA wires is zero, that is, without the SMA wires, the behavior of the SF-RCVF frame is the same as that of the SF-N frame. At point A, when the applied force returns to zero, a residual displacement remains. To eliminate this residual displacement, a reverse loading of  $-26.5$  kN from points A to B is needed. Similarly, if the frame is at point C and needs to be restored to its initial position at point D, a force of  $26.5$  kN is needed. This recentering or restoring force required is calculated using the equation

$$F_{re} = (D_{max} - D_{cr}) * K_{SF-N} = 26.5 \text{ kN}. \quad (10)$$

As  $A_{SMA}$  increases, it can be seen from Figure 9(c) that its effect becomes more prominent, and when a large  $A_{SMA}$  is used, the force-displacement relationship of the SF-RCVF frame as shown in Figure 9(d) is dominated by the SMA wires, and the residual displacements at the end of both cycles are almost zero.

To provide further insight into the restoring force provided by the SMA wires, the Wilde's SMA uniaxial constitutive model is simplified into a piecewise linear function shown in Figure 10. Part of the unloading curve is highlighted with a broken red line in Figure 10(a). For a large portion of the unloading curve, the recentering stress is larger than  $140$  MPa, which is the unloading "yield" stress  $Y_M$  of SMA. By ignoring the small strain ranging from  $-0.003$  to  $0.003$  where the SMA stress drops below  $140$  MPa, we can further idealize the unloading curve into the one shown in Figure 10(b). Within the strain range  $-0.06$  to  $0.06$ , the minimum recentering stress from the SMA wires is  $Y_M A_{SMA}$ . This is the stress that can be relied upon to pull the structure back to its original position and drastically reduce the residual displacements caused by inelastic deformation.

If  $Y_M A_{SMA}$  of the SMA wires exceeds the restoring force required by the SF-N frame, drastic reduction in residual

FIGURE 11: Residual displacements in SF-RCVF as a function of  $D_{max}$  and  $Y_M A_{SMA} / F_{cr}$ .

displacement of SF-RCVF frame can be expected. That is, when

$$Y_M A_{SMA} > F_{re} \longrightarrow \frac{Y_M A_{SMA}}{F_{cr}} > \frac{F_{re}}{F_{cr}} = 0.54, \quad (11)$$

the residual displacement can approach zero. This is reflected in Figure 9(a), which shows that as  $Y_M A_{SMA} / F_{cr}$  exceeds  $0.54$ , the residual displacement is drastically reduced and tends toward zero.

In the above discussion,  $D_{max}$  is arbitrarily set at  $60$  mm. To investigate the effect of  $D_{max}$  on the residual displacement of the SF-RCVF frame, plots similar to those of Figure 9(a) are shown in Figure 11 for a range of  $D_{max}$  from  $40$  mm to  $100$  mm. As can be seen from these figures, regardless of the value of  $D_{max}$ , the residual displacement decreases with increasing  $A_{SMA}$ , and when  $Y_M A_{SMA} / F_{cr}$  is larger than  $1$ , the residual displacement becomes negligible.

TABLE 3: Initial lateral stiffness, initial natural period/frequency, and damping coefficient of shear frames used for the time history analyses.

| Frame   | Initial lateral stiffness ( $\times 10^6$ N/m) | Initial natural period (s) | $\omega_n$ (rad/s) | $c$ (kN-s/m) |
|---------|--|----------------------------|--------------------|--------------|
| SF-N    | 1.255  | 0.335                      | 18.76              | 2.67         |
| SF-RCVF | 12.13  | 0.1077                     | 58.34              | 62.38        |
| SF-RC   | 12.13  | 0.1077                     | 58.34              | 8.32         |
| SF-VF   | 1.255  | 0.335                      | 18.76              | 20.06        |

TABLE 4: Ground motion characteristics.

| Record  | Earthquake magnitude range | Duration range (s) | Peak ground acceleration range ( $\text{cm/s}^2$ ) |
|---------|----------------------------|--------------------|--|
| LA01–20 | 6.0~7.3                    | 14.945~79.98       | 230.08~999.43                                      |
| LA21–40 | 6.7~7.4                    | 14.945~59.98       | 409.95~1304.1                                      |
| LA41–60 | 5.7~7.7                    | 26.14~79.98        | 109.45~775.05                                      |

## 6. Nonlinear Time History Analysis of Shear Frames

In this section, nonlinear dynamic time history analyses will be performed on the shear frames shown in Figure 7 to study the performance of these frames under seismic loading and to demonstrate the effectiveness of the hybrid SMA device in providing recentering and energy dissipation capabilities to the frame. For purpose of comparison, the peak story displacement or drift (PSD) will be used to evaluate the energy dissipation capacity of the frames, and the residual story drift (RSD) will be used to evaluate their recentering capacity.

Based on the nonlinear quasistatic analysis described in the preceding section, the hybrid device used for the SF-RCVF frame will have SMA wires with length of 800 mm and cross-sectional area of  $100 \text{ mm}^2$ . This corresponds to a ( $Y_M A_{\text{SMA}}/F_{cr}$ ) value of approximately 0.3.

For a single degree-of-freedom system, the damping coefficient  $c$  of the frames is calculated using equation  $c = 2\zeta m \omega_n$ , where  $\zeta$  is the specified damping ratio (or percent of critical damping) of 15%, as recommended by Dicleli and Mehta [25] for the frames with the viscous damper, and 2% for the frames without the viscous damper,  $m$  is the seismic weight, and  $\omega_n$  is the natural frequency.

The SF-RC frame is the same as the SF-RCVF frame except that it does not have the viscous fluid damper, but it does have an inherent structural damping ratio of 2%. The SF-VF frame does not have any SMA wires, but it has viscous damper with a damping ratio of 15%. The SF-N frame does not have the SMA wires or the viscous damper. It only has an inherent structural damping ratio of 2%. Using a seismic weight of 3564 kg and initial lateral stiffness computed from a quasistatic analysis and shown in the second column of Table 3, the initial natural periods, the initial natural frequencies  $\omega_n$ , and the damping coefficients  $c$  are calculated and summarized in the third, fourth, and last columns of Table 3, respectively. It should be noted that the presence of the viscous fluid damper does not have any effect on the initial stiffness of the frames. As a result, the initial stiffness and the initial natural periods of the SF-N and SF-VF frames as well as those of the SF-RCVF and SF-RC frames are the same.

The frames are assumed to be located in downtown Los Angeles on stiff soil of site class D. The ground motion histories used in the nonlinear dynamic analyses were developed for the SAC Joint Venture Steel Project Phase 2 [27, 28]. The earthquake suites corresponding to downtown Los Angeles were selected for seismic hazard levels that correspond to 50%, 10%, and 2% probability of exceedance in a 50-year period. Each suite contains 20 ground motion records, designated as LA41–LA60 for seismic ground motions with a 50% of exceedance in 50 years (frequent earthquakes), LA01–LA20 for a 10% of exceedance in 50 years (rare earthquakes), and LA21–LA40 for a 2% of exceedance in 50 years (very rare earthquakes), respectively. These 60 records were derived from fault-parallel and fault-normal orientations of 30 earthquake records with adjustment in amplitude and frequency domain. Some ground motion characteristics for these earthquakes are summarized in Table 4.

In a nonlinear time history analysis, the equation of motion given below is solved:

$$m\ddot{u} + c\dot{u} + ku = -m\ddot{u}_g. \quad (12)$$

In the above equation,  $m$  is the mass or seismic weight of the structural system,  $c$  is the damping coefficient,  $k$  is the system stiffness,  $u$ ,  $\dot{u}$ , and  $\ddot{u}$  are the displacement, velocity, and acceleration of the structural system, and  $\ddot{u}_g$  is the ground acceleration of the specific earthquake. Because the system stiffness  $k$  varies with time, the above equation is often expressed in incremental form and solved using a numerical technique that entails iteration. In the present analysis, the incremental form of the Newmark's  $\beta$  method [29] is used. A computer program written in MATLAB and verified against the example problem given in [29] was used to perform the analyses.

The roof displacements or story drifts obtained for the four shear frames of Figure 7 subjected to the LA28 (a very rare) Northridge ground motion history of Figure 12(a) are shown in Figure 12(b). This ground motion has a peak ground acceleration of  $13.04 \text{ m/s}^2$  or about 1.33 g. For each frame, the peak story drift (PSD) is obtained as the maximum displacement ordinate from the plot, and the residual story drift (RSD) is obtained as the displacement ordinate when

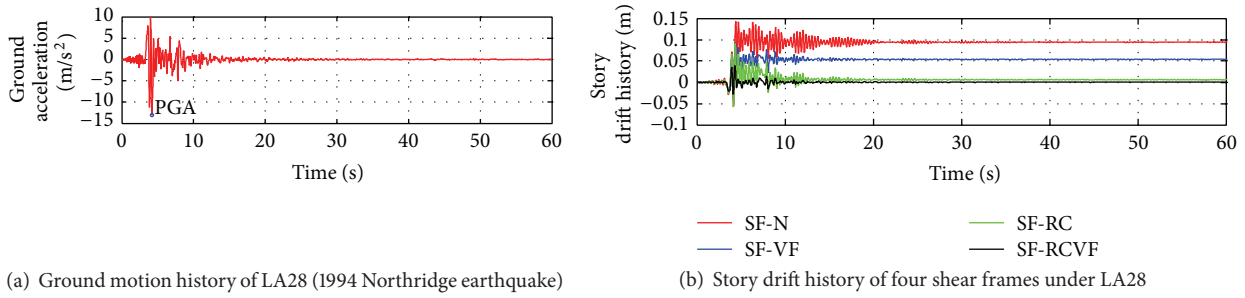


FIGURE 12: Time history analysis of four shear frames under LA28 (1994 Northridge earthquake).

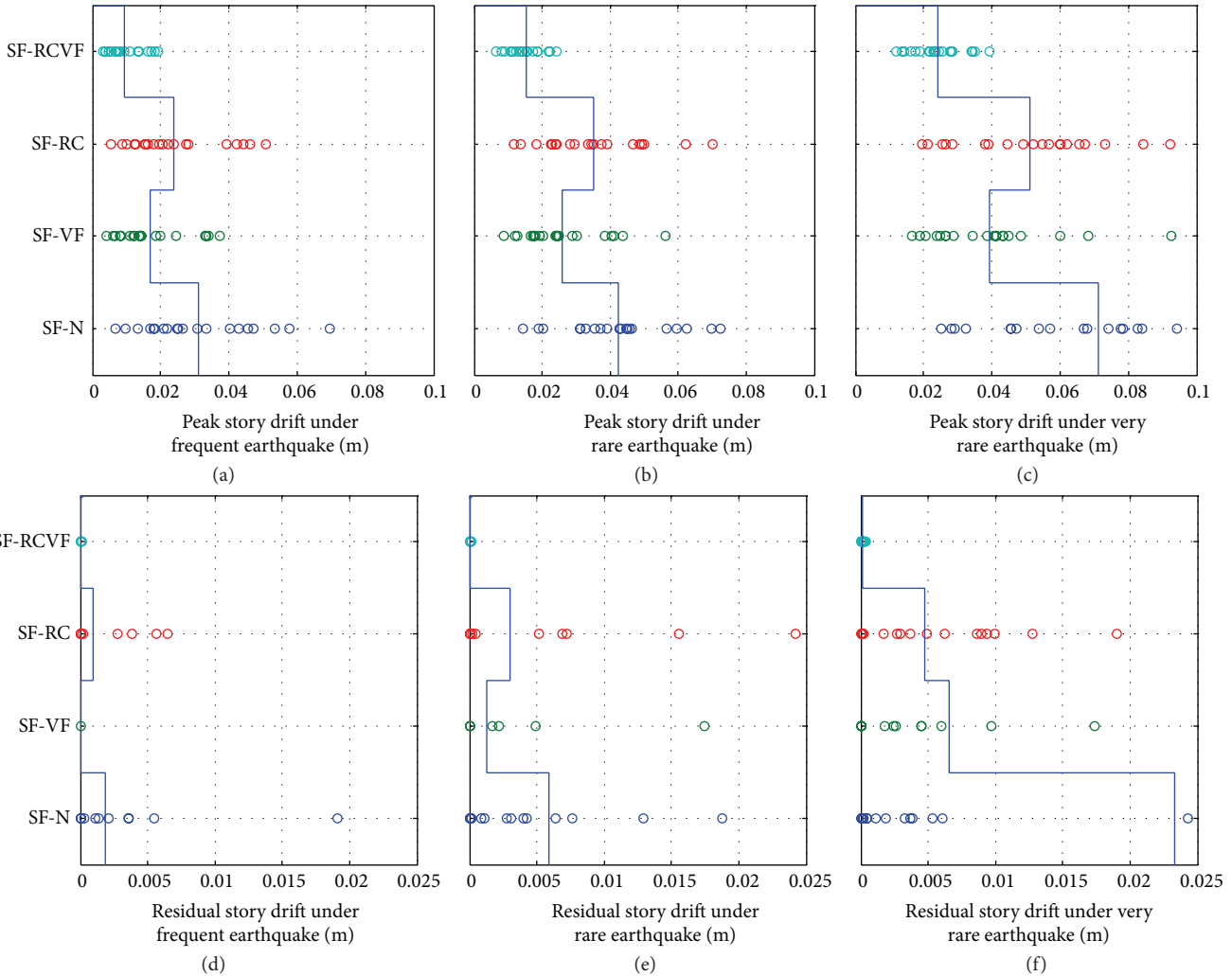


FIGURE 13: Peak and residual story drifts of four shear frames under three levels of earthquake excitations.

vibration has subsided. From Figure 12(b), it can be seen that the SF-RCVF frame has a PSD less than 0.04 m, with a negligible residual story drift. On the other hand, the SF-N frame has a rather large PSD of approximately 0.145 m and a RSD slightly less than 0.1 m. By comparing the PSD and RSD of the SF-N and SF-VF frames, we can see that while the viscous fluid damper can help reduce both PSD and RSD, a noticeable RSD remains. As for the SF-RC frame, we can see that the SMA recentering wires can greatly reduce RSD, even though its PSD is almost as large as that of the SF-VF

frame. For a given member stiffness, the internal forces and moments are proportional to member deformations. As a result, the small story drift experienced by SF-RCVF means its members will have the lowest shear force and moment, and the frame will have the best chance of maintaining its structural integrity in a very rare earthquake.

The analysis is carried out for all 60 earthquake records for the four frames. The results are summarized in Figure 13, where the peak and residual story drifts under the aforementioned three levels of ground excitations are plotted.

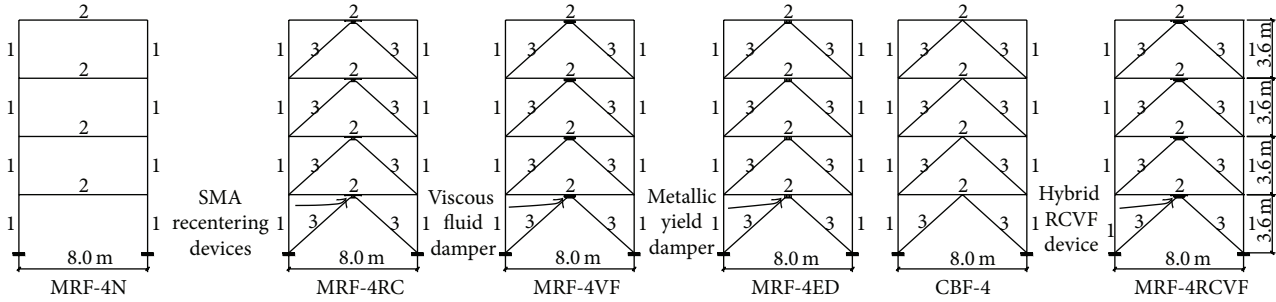


FIGURE 14: Four-story steel frames.

The three levels are designated as frequent, rare, and very rare earthquakes, respectively. Because each suite of ground motions contains 20 earthquake records, the drift result from a specific earthquake is shown as an open circle while their mean values are shown as solid vertical lines. It should be noted that, in order to keep the size of the axis the same for easier comparison, some circles that fall outside of the indicated frame size are not shown in the figures.

From the figures, it can be seen that as earthquake intensity increases, both the peak story drift (PSD) and the residual story drift (RSD) increase. With no SMA or VF, the SF-N frame has mean PSD values of 0.031 m, 0.042 m, and 0.071 m for the three levels of earthquakes, respectively. The corresponding mean RSD values are 0.002 m, 0.007 m, and 0.024 m. While the drift performance of this frame under frequent to rare earthquake is acceptable with a maximum PSD value of 0.072 m that corresponds to a drift ratio of 2%, 10 out of 20 earthquakes at the very rare level give PSD values that exceed the 2% drift ratio, with the maximum PSD as high as 0.184 m corresponding to a drift ratio of 5.1% for the LA 31 Elysian Park record.

The use of only the viscous fluid damper (frame SF-VF) or the SMA recentering wires (frame SF-RC) can noticeably reduce both PSD and RSD. However, by comparing the RSD values of the SF-RC and SF-RCVF frames shown in Figures 13(d) to 13(f), one can see that the recentering effect of the SMA wires is not fully realized without the viscous fluid damper. From Figures 13(d) and 13(e) for frequent and rare earthquakes, one can see that the mean RSD value of the SF-VF frame is actually lower than that of the SF-RC frame, which seems to suggest that the use of the viscous damper alone is sufficient to significantly reduce or even eliminate residual displacements. However, based on a study by Dicleli and Mehta [25] on concentrically braced frames with large number of stories subjected to high intensity ground motions, the effectiveness of using viscous fluid dampers with damping ratio exceeding 30% is not particularly effective in enhancing structural seismic performance. Thus, relying on viscous fluid dampers alone is neither an effective nor economic approach to reduce RSD. In the present analysis, the mean RSD value for the SF-VF frame under the excitation of the suite of very rare earthquakes is 0.0066 m. The maximum RSD is 0.054 m, which corresponds to a story drift ratio of 1.5%.

Compared with the other three shear frames, the performance of the SF-RCVF frame is noticeably better in terms

TABLE 5: Peak and residual story drifts of SF-RCVF and SF-VF under very rare earthquake.

|     | SF-RCVF | SF-VF |
|-----|---------|-------|
| PSD | 24 mm   | 39 mm |
| RSD | 0.1 mm  | 7 mm  |

of both PSD and RSD. The maximum PSD value under very rare earthquake in this analysis is less than 0.04 m (1.2% drift ratio), and the mean RSD value is negligible. The expected synergistic effect of recentering and energy dissipation is realized. Although the hybrid device contains only 100 mm<sup>2</sup> of SMA wires, the reduction of PSD and RSD in the SF-RCVF frame from the SF-VF frame is rather significant, as shown in Table 5.

## 7. Analysis of Four-Story Steel Frames

To further demonstrate the effectiveness of the proposed hybrid device in mitigating earthquake damage to buildings, a series of six four-story steel frames as shown in Figure 14 are analyzed using the same ground motion records applied earlier for the time history analysis of the shear frames. The abbreviation MRF-4 refers to these 4-story steel frames. The letters N, RC, VF, ED, and RCVF denote frames (1) without the use of any device, (2) with the use of the recentering device (i.e., the SMA wires) only, (3) with the use of the viscous fluid damper only, (4) with the use of an elastoplastic (i.e., metallic yielding) damper only, and (5) with the use of both the recentering device and the viscous fluid damper (i.e., the proposed hybrid device), respectively. The numbers (1, 2, 3) on the members correspond to steel sections given in Table 6. For purpose of comparison, an additional frame labelled CBF-4, which is a regular chevron-braced frame, will also be analyzed.

Except for MRF-4N, the braces for all the frames are modeled using a brace model proposed by Higginbotham and Hanson [30]. The Higginbotham-Hanson model is capable of modeling the hysteretic behavior, including buckling strength deterioration, of a brace under repeated tension-compression cycles. In the present analysis, brace buckling is said to have occurred when its axial force is equal to or exceeds the compressive axial strength of the member as per the AISC specification [31].

TABLE 6: Cross-sectional properties of steel members.

| Member number | Member designation               | Cross-sectional area<br>$A$ (mm <sup>2</sup> ) | Moment of inertia<br>$I_x$ ( $\times 10^6$ mm <sup>4</sup> ) | Plastic section modulus<br>$Z_x$ ( $\times 10^3$ mm <sup>3</sup> ) |
|---------------|----------------------------------|--|--|--|
| 1             | W310 $\times$ 202*               | 25,700   | 516  | 3,507  |
| 2             | W310 $\times$ 158*               | 20,100   | 388  | 2,687  |
| 3             | HSS203 $\times$ 203 $\times$ 8** | 5,650  | 35.7   | 412  |

\* A36 steel ( $F_y = 248$  MPa,  $E = 200$  GPa).

\*\* A500 Grade B steel ( $F_y = 318$  MPa,  $E = 200$  GPa).

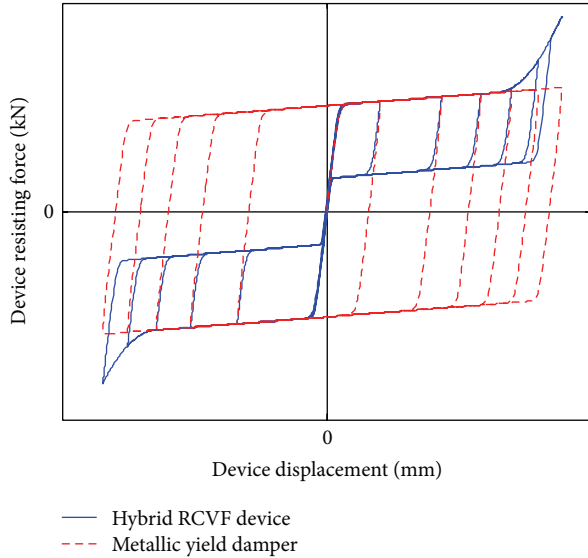


FIGURE 15: Assumed force-displacement relationship for the metallic damper.

To provide a meaningful comparison, the force-displacement relationship of the metallic yield damper used for MRF-4ED is adjusted so its initial stiffness and hardening stiffness are the same as those of the SMA wires and its yield strength is assumed to be identical to that of the SMA forward transformation strength  $Y_A A_{SMA}$  as shown in Figure 15.

The seismic weight used for each story of all the frames and the initial fundamental frequency  $\omega_1$ , damping ratio  $\zeta_1$ , and damping coefficients  $c_j$  used for each of the six frames are given in Tables 7 and 8, respectively.

Using a lumped mass model in which the seismic weight of a given story is lumped at midspan of the beam, nonlinear time history analysis was performed for each frame using the sixty ground motion records. The results for the peak top story displacements and the peak interstory drift ratios as well as the residual top story displacements and the residual interstory drift ratios for the six frames are shown and compared in Figures 16, 17, 18, and 19. In these figures, the actual data points are shown as open circles and the lines represent their average values.

From these figures, the following can be seen.

- (1) Except for CBF-4, the MRF-4RCVCF frame experiences the least peak top story displacements and peak interstory drifts. Although chevron braces are often used for seismic retrofitting and it has been shown

TABLE 7: Seismic weight for each story.

| Story | Seismic weight (Kg) |
|-------|---------------------|
| 4     | 28113               |
| 3     | 33542               |
| 2     | 33542               |
| 1     | 33542               |

TABLE 8: Frame dynamic properties.

| Frame      | $\omega_1$ (rad) | $\zeta_1$ | $c_j$ (kN-s/m) |
|------------|------------------|-----------|----------------|
| MRF-4N     | 6.67             | 2%        | 61.5           |
| MRF-4RC    | 13.65            | 2%        | 137.4          |
| MRF-4VF    | 6.67             | 15%       | 461.2          |
| MRF-4ED    | 13.65            | 2%        | 137.4          |
| CBF-4      | 22.73            | 2%        | 229.5          |
| MRF-4RCVCF | 13.65            | 15%       | 1030.2         |

from nonlinear pushover analysis [32] that frame displacements can be significantly reduced, chevron-braced frames (CBF) often have low ductility [33] and unless properly designed or special braces such as the buckling restrained braces [34] are used, the frame capacity is usually limited by the buckling capacity of the braces. Indeed, some brace members in the lower stories of the CBF-4 frame were found to have experienced buckling, while no such brace failure occurred in the MRF-4RCVCF frame.

- (2) Regardless of the severity level of the earthquakes, both the peak top story displacement and peak inter-story drifts of the MRF-4RCVCF frame fall within the limits specified by FEMA 356 [35] for life safety and collapse prevention. Also, small displacements mean members of this frame will experience low internal forces and moments, and the frame equipped with the proposed hybrid device is most likely to maintain its structural integrity after these earthquakes.
- (3) Except under very rare earthquakes, the residual top story displacement and the residual interstory drifts for the MRF-4RCVCF frame are almost negligible indicating that the frame remains more-or-less elastic under these levels of earthquakes. The frame is therefore the most suitable for immediate occupancy after a frequent or rare earthquake.

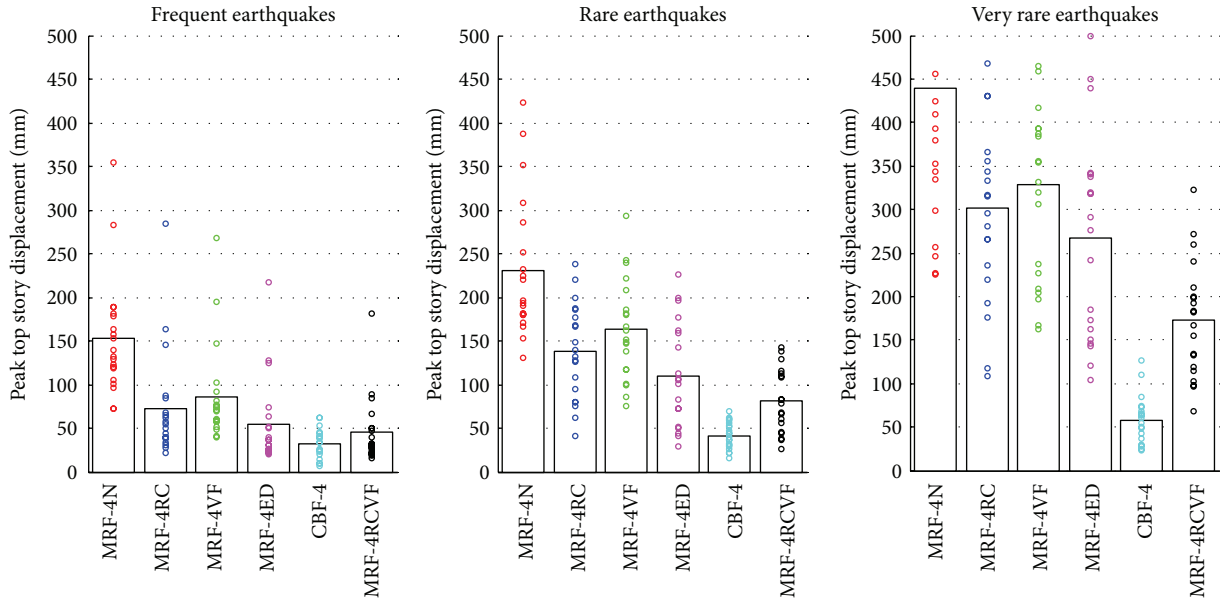


FIGURE 16: Peak top story displacements.

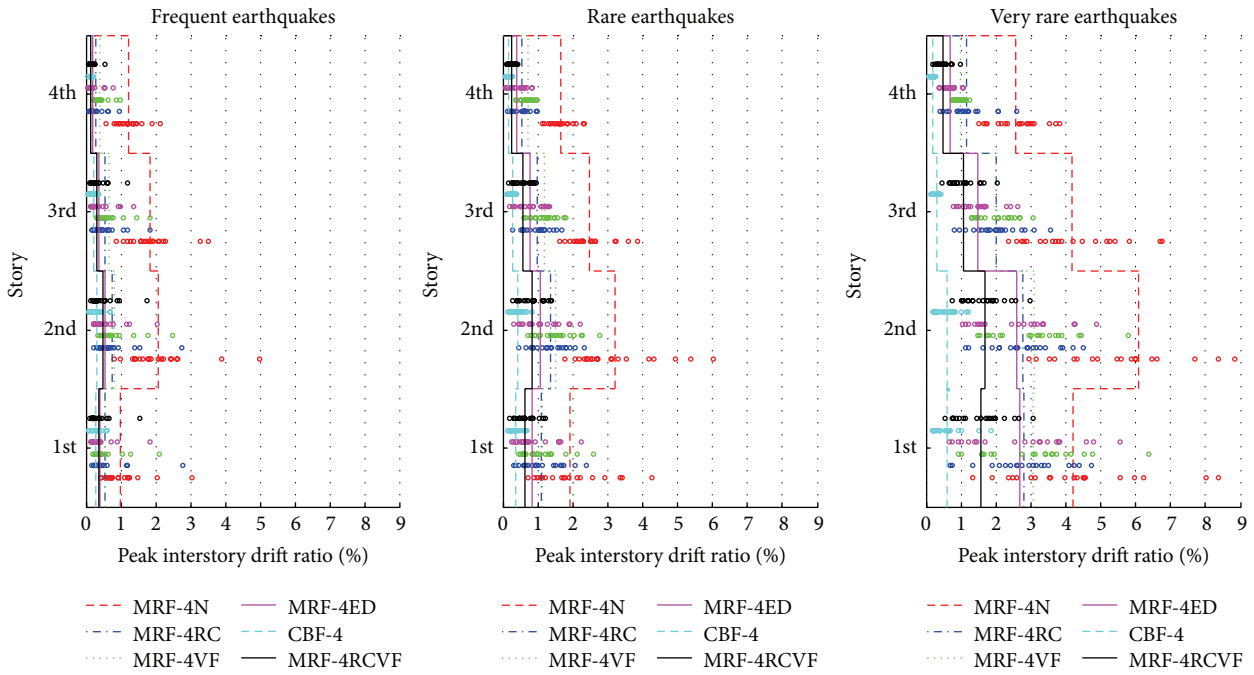


FIGURE 17: Peak interstory drift ratios.

### 8. Conclusions

In this paper, a hybrid device was proposed to enhance the recentering and energy dissipation capabilities of frames designed in the context of performance-based criteria. Recentering and energy dissipation are provided by the two components—SMA wires and a viscous fluid damper—of the device, respectively.

Nonlinear quasistatic analysis was performed on four shear frames, and nonlinear time history analysis was conducted on these shear frames as well as on a series of

four-story steel frames to investigate the effectiveness of the proposed hybrid device. In the numerical study, the behavior of the SMA wires was modeled using Wilde’s constitutive model and the viscous fluid damper was simulated using the linear Maxwell model. The results obtained from the present study are summarized below as follows.

- (1) From the nonlinear quasistatic analysis, it has been found that, as long as the recentering force is larger than the plastic limit force of the frame, near

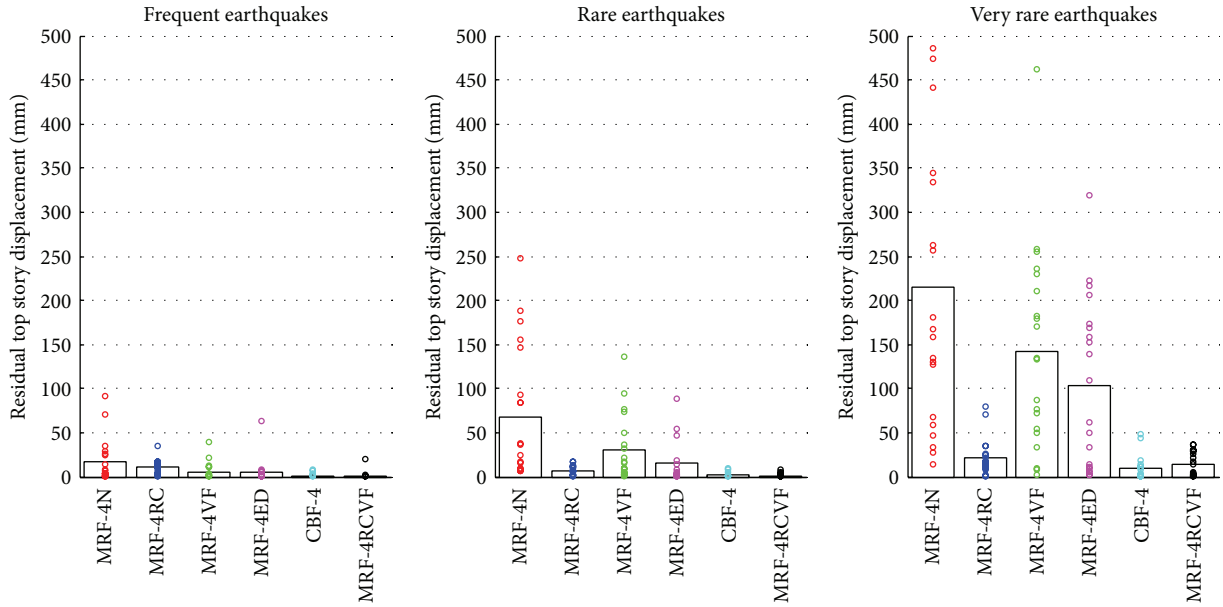


FIGURE 18: Residual top story displacements.

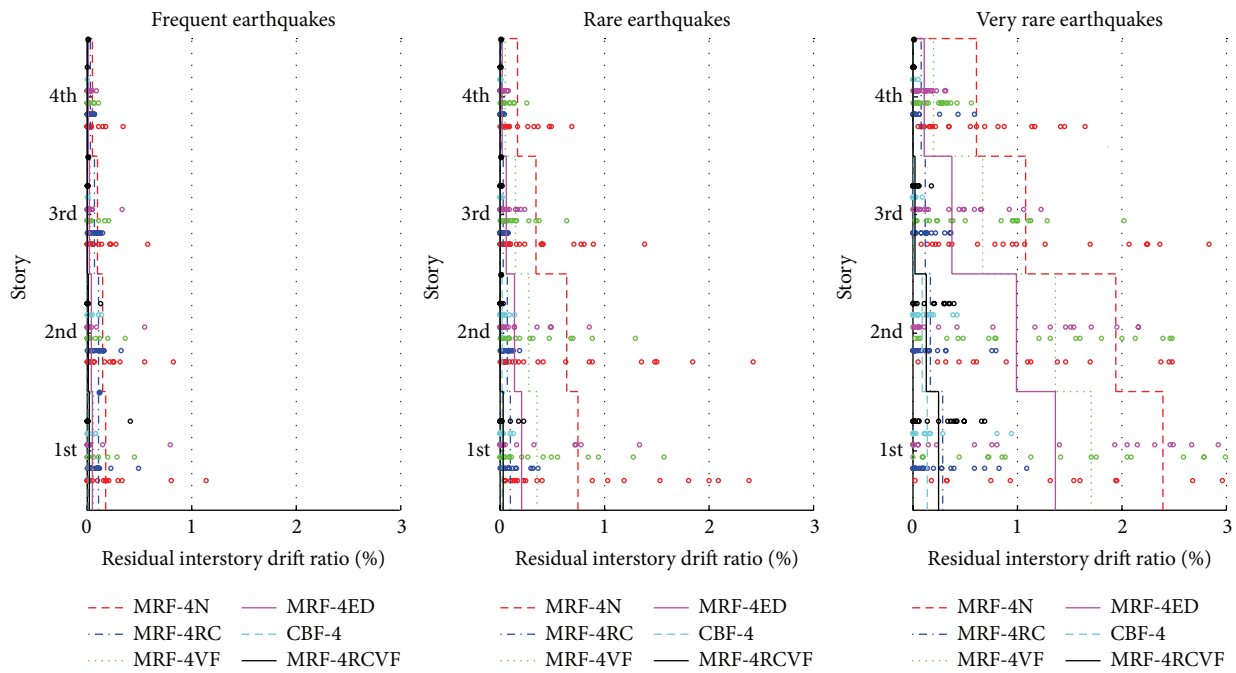


FIGURE 19: Residual interstory drift ratios.

complete recentering can be achieved even after inelastic deformations have occurred.

- (2) From the nonlinear quasistatic analysis, it can be concluded that viscous fluid dampers, whose force is velocity dependent, do not exert any residual force on the frame to undercut the recentering force from the SMA wires. As a result, the full recentering effect of the SMA wires can be utilized.
- (3) From the nonlinear time history analysis, it can be seen that although the SMA wires can, by themselves,

reduce the residual drift of the frame, the peak story drift could remain large. On the other hand, although the viscous fluid damper by itself can reduce the frame's peak story drift, the residual drift is still noticeably present, especially when the frame is subjected to very rare earthquake events.

- (4) The synergistic effect of the hybrid device can significantly reduce both the peak and residual story drifts and has the potential to bring the frame back to its preearthquake configuration for frequent and rare earthquakes.

- (5) Frames equipped with the proposed hybrid device are capable of maintaining their structural integrity under all levels of earthquakes and are suitable for immediate occupancy under frequent and rare earthquakes.

### Conflict of Interests

The authors declare that there is no conflict of interests regarding the publication of this paper.

### References

- [1] W. M. Ghannoum, J. P. Moehle, and Y. Bozorgnia, "Analytical collapse study of lightly confined reinforced concrete frames subjected to northridge earthquake ground motions," *Journal of Earthquake Engineering*, vol. 12, no. 7, pp. 1105–1119, 2008.
- [2] M. Bruneau, J. C. Wilson, and R. Tremblay, "Performance of steel bridges during the 1995 Hyogo-ken Nanbu (Kobe, Japan) earthquake," *Canadian Journal of Civil Engineering*, vol. 23, no. 3, pp. 678–713, 1996.
- [3] I. G. Buckle, *The Northridge California Earthquake of January 17, 1994: Performance of Highway Bridges*, National Center for Earthquake Engineering Research, Buffalo, NY, USA, 1994.
- [4] FEMA P-750, "Recommended seismic provisions for new buildings and other structures," Building Seismic Safety Council of the National Institute of Building Sciences, Washington, DC, USA, 2009.
- [5] SEAOC, *Vision2000, performance based seismic engineering of buildings, vols. I and II: conceptual framework*, Sacramento, Calif, USA, Structural Engineers Association of California, 2000.
- [6] J. Dong, C. S. Cai, and A. M. Okeil, "Overview of potential and existing applications of shape memory alloys in bridges," *Journal of Bridge Engineering*, vol. 16, no. 2, pp. 305–315, 2011.
- [7] J. van Humbeeck and S. Kustov, "Active and passive damping of noise and vibrations through shape memory alloys: applications and mechanisms," *Smart Materials and Structures*, vol. 14, no. 5, pp. S171–S185, 2005.
- [8] D. Shook, P. Roschke, P. Y. Lin, and C. H. Loh, "Experimental investigation of super-elastic semi-active damping for seismically excited structures," in *Proceedings of the 18th Analysis and Computation Specialty Conference*, Vancouver, Canada, 2008.
- [9] S. Zhu and Y. Zhang, "Seismic analysis of concentrically braced frame systems with self-centering friction damping braces," *Journal of Structural Engineering*, vol. 134, no. 1, pp. 121–131, 2008.
- [10] C.-S. W. Yang, R. DesRoches, and R. T. Leon, "Design and analysis of braced frames with shape memory alloy and energy-absorbing hybrid devices," *Engineering Structures*, vol. 32, no. 2, pp. 498–507, 2010.
- [11] D. J. Miller, L. A. Fahnestock, and M. R. Eatherton, "Self-centering buckling-restrained braces for advanced seismic performance," in *Proceedings of the ASCE Structures Congress*, pp. 960–970, Las Vegas, Nev, USA, April 2011.
- [12] D. E. Hodgson, M. H. Wu, and R. J. Biermann, "Shape memory alloys," in *ASM Handbook: Volume 2: Properties and Selection: Nonferrous Alloys and Special-Purpose Materials*, pp. 897–902, 1990.
- [13] O. E. Ozbulut, S. Hurlbaas, and R. DesRoches, "Seismic response control using shape memory alloys: A review," *Journal of Intelligent Material Systems and Structures*, vol. 22, no. 14, pp. 1531–1549, 2011.
- [14] J. M. Gong, H. Tobushi, K. Takata, and K. Okumura, "Superelastic deformation of a TiNi shape memory alloy subjected to various cyclic loadings," *Journal of Materials Design and Applications*, vol. 216, no. 1, pp. 17–23, 2002.
- [15] M. Dolce, D. Cardone, and R. Marnetto, "Implementation and testing of passive control devices based on shape memory alloys," *Earthquake Engineering & Structural Dynamics*, vol. 29, no. 7, pp. 945–968, 2000.
- [16] H. Li, M. Liu, and J. P. Ou, "Vibration mitigation of a stay cable with one shape memory alloy damper," *Structural Control and Health Monitoring*, vol. 28, no. 9, pp. 1–36, 2004.
- [17] B. Andrawes and R. DesRoches, "Unseating prevention for multiple frame bridges using superelastic devices," *Smart Materials and Structures*, vol. 14, no. 3, pp. S60–S67, 2005.
- [18] E. J. Graesser and F. A. Cozzarelli, "Proposed three-dimensional constitutive model for shape memory alloys," *Journal of Intelligent Material Systems and Structures*, vol. 5, no. 1, pp. 78–89, 1994.
- [19] K. Wilde, P. Gardoni, and Y. Fujino, "Base isolation system with shape memory alloy device for elevated highway bridges," *Engineering Structures*, vol. 22, no. 3, pp. 222–229, 2000.
- [20] H. Qian, H. N. Li, and G. Song, "A constitutive model of shape memory alloys with consideration of martensitic hardening effect," in *Earth & Space*, pp. 1–8, American Society of Civil Engineers, Long Beach, Calif, USA, 2008.
- [21] Y. Zhang and S. Zhu, "A shape memory alloy-based reusable hysteretic damper for seismic hazard mitigation," *Smart Materials and Structures*, vol. 16, no. 5, pp. 1603–1613, 2007.
- [22] M. C. Constantinou and M. D. Symans, "Experimental and analytical investigation of seismic response of structures with supplemental fluid viscous dampers," Tech. Rep. NCEER-92-0032, National Center for Earthquake Engineering Research, State University of New York, Buffalo, NY, USA, 1992.
- [23] M. Martinez-Rodrigo and M. L. Romero, "An optimum retrofit strategy for moment resisting frames with nonlinear viscous dampers for seismic applications," *Engineering Structures*, vol. 25, no. 7, pp. 913–925, 2003.
- [24] P. Uriz and A. S. Whittaker, "Retrofit of pre-northridge steel moment-resisting frames using fluid viscous dampers," *The Structural Design of Tall Buildings*, vol. 10, no. 5, pp. 371–390, 2001.
- [25] M. Dicleli and A. Mehta, "Seismic performance of chevron braced steel frames with and without viscous fluid dampers as a function of ground motion and damper characteristics," *Journal of Constructional Steel Research*, vol. 63, no. 8, pp. 1102–1115, 2007.
- [26] American Society of Civil Engineers, *ASCE 7-10, Minimum Design Loads for Buildings and Other Structures*, American Society of Civil Engineers, Reston, Va, USA, 2010.
- [27] P. G. Sommerville, N. F. Smith, S. Punyamurthula, and J. I. Sun, "Development of ground motion time histories for phase 2 of the FEAM/SAC steel project," SAC Background Document SAC/BD-91/04, SAC Joint Venture, Sacramento, Calif, USA, Sacramento, 1997.
- [28] Woodward-Clyde Federal Services, "Project Title: Develop Suites of Time Histories," SAC Joint Venture Steel Project Phase 2, 1997, [http://nisee.berkeley.edu/data/strong\\_motion/sacsteel/draftreport.html](http://nisee.berkeley.edu/data/strong_motion/sacsteel/draftreport.html).
- [29] A. K. Chopra, *Dynamics of Structures: Theory and Applications to Earthquake Engineering*, Prentice Hall, Englewood Cliffs, NJ, USA, 4th edition, 2012.

- [30] A. B. Higginbotham and R. D. Hanson, "Axial hysteretic behavior of steel members," *Journal of the Structural Division*, vol. 102, no. 7, pp. 1365–1381, 1976.
- [31] AISC, *Manual of Steel Construction: Load and Resistance Factor Design*, American Institute of Steel Construction, Chicago, Ill, USA, 14th edition, 2011.
- [32] H. A. Safarizki, S. A. Kristiawan, and A. Basuki, "Evaluation of the use of steel bracing to improve seismic performance of reinforced concrete building," *Procedia Engineering*, vol. 54, pp. 447–456, 2013.
- [33] E. A. Godínez-Domínguez, A. Tena-Colunga, and L. E. Pérez-Rocha, "Case studies on the seismic behavior of reinforced concrete chevron braced framed buildings," *Engineering Structures*, vol. 45, pp. 78–103, 2012.
- [34] G. Abdollahzadeh and M. Banihashemia, "Response modification factor of dual moment-resistant frame with buckling restrained brace (BRB)," *Steel and Composite Structures*, vol. 14, no. 6, pp. 621–636, 2013.
- [35] FEMA 356, *Prestandard and Commentary for the Seismic Rehabilitation fo Buildings*, Federal Emergency Management Agency, Washington, DC, USA, 2000.



**Hindawi**

Submit your manuscripts at  
<http://www.hindawi.com>

